

# Magnetic and Thermal Properties of $\text{SmRh}_2\text{Zn}_{20}$ Single Crystal

Yosikazu Isikawa\*, Toshio Mizushima, Aika Fujita, and Tomohiko Kuwai

*Graduate School of Science and Engineering, University of Toyama, Toyama 930-8555,  
Japan*

The magnetization, magnetic susceptibility, and specific heat of the single crystalline sample  $\text{SmRh}_2\text{Zn}_{20}$  were measured. The valence of Sm ions in  $\text{SmRh}_2\text{Zn}_{20}$  was found to be trivalent. No evidence of valence fluctuations was detected.  $\text{SmRh}_2\text{Zn}_{20}$  is an antiferromagnet with  $T_N = 2.46$  K. The observed magnetic phase transition temperature in the  $C(T, H)$  curves showed that  $T_N$  splits into two in the external field  $H$  along the  $[001]$  and  $[101]$  directions. On the other hand,  $T_N$  in  $H$  along the  $[111]$  direction did not split, decreasing to 2.20 K at  $H = 7$  T. At 2 K, the magnetization  $M_{111}$  in  $H$  along the  $[111]$  direction increased linearly with increasing field, while  $M_{001}$  and  $M_{101}$  deviated upward slightly from the linear dependence. We analyzed the observed magnetic and thermal properties of  $\text{SmRh}_2\text{Zn}_{20}$  taking into account the crystalline-electric-field effect, the Zeeman energy, and the exchange interaction. The theoretical calculation well reproduced the experimental  $\chi(T)$ ,  $M(H)$ ,  $C(T, H)$  and  $T_N(H)$ , suggesting that the energy scheme of  $\text{Sm}^{3+}$  is composed of the ground state  $\Gamma_7$  and the excited state  $\Gamma_8$  with an energy gap of 10.8 K. The sublattice magnetic moments are expected to be along the  $\langle 111 \rangle$  direction below  $T_N$  at  $H = 0$  T. Variations of the magnetic structures induced by the external magnetic fields in a narrow temperature region around  $T_N$  are inferred on the basis of theoretical calculations.

## 1. Introduction

Many Sm-based compounds have been investigated for more than three decades because they show the fundamental physical properties of condensed matters such as valence fluctuation and intermediate valence.<sup>1,2)</sup> Recently,  $RTr_2X_{20}$ -type compounds ( $R$  = rare earth,  $Tr$  = transition metal,  $X$  = Al, Zn, Cd) have attracted much attention because of their various physical properties.<sup>3-8)</sup> They crystallize in the cubic structure, and the rare-earth atoms are in the cubic symmetric sites. Sakai and Nakatsuji, Higashinaka et al., and Yamada et al. presented the interesting experimental results<sup>9-11)</sup> indicating that  $\text{Sm}Tr_2\text{Al}_{20}$  ( $Tr$  = Ti, V, Cr, Ta) are an-

\*E-mail: isikawa@sci.u-toyama.ac.jp

tiferromagnets with strong valence fluctuation, which brought about characteristic behaviors such as a large electronic specific-heat coefficient  $C/T$ , a weak temperature dependence of magnetic susceptibility, a  $-\ln T$ -dependent resistivity, and a field-insensitive phase transition. The peculiar valence fluctuation is ascribed to the strong  $c$ - $f$  hybridization. It is contradictory, however, to the fact that the ground state of Sm ions in all  $\text{SmTr}_2\text{Al}_{20}$  is said to be a quartet  $\Gamma_8$  of trivalent Sm. Kuwai et al. measured<sup>12)</sup> the thermoelectric power  $S$  of  $\text{SmTr}_2\text{Al}_{20}$  ( $Tr = \text{Ti, V, Cr}$ ) and found the large values of  $\Delta S/T$  at temperatures above and near the Néel temperature  $T_N$ . The large values of  $S$  correspond approximately to the large values of  $C/T$  since  $S$  is proportional to  $C$  when both originate from the density of states of the conduction electrons at the Fermi energy.

$\text{SmTr}_2\text{Zn}_{20}$  ( $Tr = \text{Fe, Co, Ru}$ ) and  $\text{SmTr}_2\text{Cd}_{20}$  ( $Tr = \text{Ni, Pd}$ ) have been investigated by Yazici et al.<sup>13)</sup> and Jia et al.<sup>14)</sup>  $\text{SmTr}_2\text{Zn}_{20}$  ( $Tr = \text{Fe, Ru}$ ) and  $\text{SmNi}_2\text{Cd}_{20}$  exhibit ferromagnetic order, whereas  $\text{SmPd}_2\text{Cd}_{20}$  is an antiferromagnet and  $\text{SmCo}_2\text{Zn}_{20}$  is nonmagnetic down to 110 mK. The valence of Sm ions in these series is close to trivalent. The ground state of  $\text{Sm}^{3+}$  due to the crystalline-electric-field (CEF) effect is quartet  $\Gamma_8$  for  $\text{SmRu}_2\text{Zn}_{20}$ <sup>15)</sup> and  $\text{SmPd}_2\text{Cd}_{20}$ .<sup>13)</sup>  $\text{SmRu}_2\text{Zn}_{20}$  shows an anomalous magnetic anisotropy of magnetization below the Curie temperature  $T_C$ , which contradicts the anisotropy predicted from the  $\Gamma_8$  ground state.<sup>15)</sup> Isikawa et al. suggested<sup>15)</sup> the possibility of the octupole-octupole interaction as a mechanism to explain the anomalous magnetic anisotropy. Yazici et al. suggested<sup>13)</sup> that  $\text{SmRu}_2\text{Zn}_{20}$  is a rare compound of Sm-based heavy-fermion ferromagnet based on the Sommerfeld–Wilson and Kadowaki–Woods ratios.

A few experimental data revealed<sup>16–20)</sup> that  $\text{SmIr}_2\text{Zn}_{20}$  and  $\text{SmRh}_2\text{Zn}_{20}$  are antiferromagnets with  $T_N$  at 1.3 and 2.4 K, respectively. The former has an additional  $T_N$  at 1.2 K. The ground state of Sm ions is the  $\Gamma_7$  doublet for both compounds, which are rare examples among the  $\text{SmTr}_2\text{X}_{20}$ -type compounds. In  $\text{SmRh}_2\text{Zn}_{20}$ , the field-induced new phases and the field-induced first-order transition were observed. However, this first-order transition was sample-sensitive.

In this paper, we report the magnetic susceptibility  $\chi(T)$ , magnetization  $M(H)$ , and specific heat  $C(T, H)$  of  $\text{SmRh}_2\text{Zn}_{20}$  to elucidate the fundamental physical properties of the sample.  $\text{SmRh}_2\text{Zn}_{20}$  is an antiferromagnet with a Néel temperature  $T_N = 2.46$  K. The observed peak in the  $C(T)$  curve at  $T_N$  is split into two by the external field  $H$ , depending on the field direction. A phase diagram of  $T_N$  vs  $H$  is given. The experimental results of  $\chi(T)$ ,  $M(H)$ ,  $C(T, H)$ , and the field-direction dependence of  $T_N$  are well reproduced by the theoretical calculations based on the CEF effect, Zeeman effect, and exchange interaction. The variations

of the magnetic structures in  $H$  are discussed on the basis of theoretical calculations.

## 2. Experimental Procedure

Single crystals of  $\text{SmRh}_2\text{Zn}_{20}$  and the reference sample  $\text{YRh}_2\text{Zn}_{20}$  were grown by the Zn-self-flux method, which was the same as that described previously.<sup>21,22)</sup> The crystal structure of the cubic  $\text{CeCr}_2\text{Al}_{20}$  type was confirmed from the X-ray powder diffraction pattern. There was no trace of impurity phases. The lattice parameters  $a$  of  $\text{SmRh}_2\text{Zn}_{20}$  and  $\text{YRh}_2\text{Zn}_{20}$  were obtained to be 14.226 and 14.200 Å, respectively, which agree with those in the literature.<sup>23,24)</sup> The crystal axis was determined from Laue pictures. The samples were shaped using a spark-cutting machine, and the weights of the samples  $\text{SmRh}_2\text{Zn}_{20}$  and  $\text{YRh}_2\text{Zn}_{20}$  are 4.46 and 7.67 mg, respectively, which were used for all the measurements. We recognized a sample dependence of the physical properties in  $\text{SmRh}_2\text{Zn}_{20}$ ; thus, we present here the data of the sample, the specific heat  $C(T)$  of which shows the sharpest peak at  $T_N$  and the highest  $T_N$ .

The magnetization  $M$  and the magnetic susceptibility  $\chi$  were measured at temperatures down to 2.0 K using a magnetic property measurement system (MPMS, Quantum Design Inc.). The specific heat was measured at temperatures down to 0.5 K using a physical property measurement system (PPMS, Quantum Design Inc.).

## 3. Experimental Results

Figure 1 shows the temperature dependence of the magnetic susceptibility of  $\text{SmRh}_2\text{Zn}_{20}$  in the field 1 T along the [001] direction. The value of  $\chi$  at 300 K suggests that the Sm ions in  $\text{SmRh}_2\text{Zn}_{20}$  are in the trivalent state, not in the valence-mixing state.<sup>1)</sup> The magnetism of the trivalent Sm compound is generally expressed by the sum of two components: the Curie term that originated from  $J = 5/2$  and the Van Vleck term that originated from the mixing of  $J = 5/2$  with  $7/2$ , that is,  $\chi^{3+}(T) = C/T + \chi_{\text{VV}}$ , where  $C$  is the Curie constant of  $J = 5/2$ . In addition, the magnetic susceptibility is affected by the exchange interaction as follows:  $1/\chi = 1/\chi^{3+} - n$ . The solid line in Fig. 1 shows the calculated  $\chi(T)$  curve using the two parameters,  $\chi_{\text{VV}} = 0.97 \times 10^{-3}$  emu/mol and  $n = -47$  mol/emu. The experimental susceptibility is in good agreement with the calculated one. The inset in Fig. 1 shows the reciprocal susceptibility  $1/\chi$  and corrected reciprocal susceptibility  $1/(\chi(T) - \chi_{\text{VV}})$  at temperatures below 30 K in the same field as in the main figure. The corrected susceptibility shows a linear dependence of temperature representing the usual Curie–Weiss law. The thick solid line in the inset is the calculated line using  $n$ . At low temperatures between 3 and 30 K, the experimental data is also in good agreement with the calculated one. The good agreement at temperatures between 3

and 300 K indicates that the CEF effect is small. The paramagnetic Curie temperature  $\theta_p$  was deduced to be  $-5$  K from the data in Fig. 1, which is related theoretically to the parameter  $n$  as  $\theta_p = nC$ .

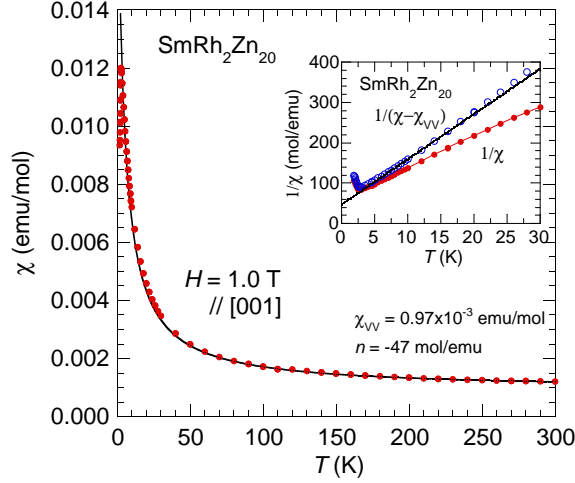


**Fig. 1.** (Color online) Magnetic susceptibility of  $\text{SmRh}_2\text{Zn}_{20}$  in the field 1 T along the [001] direction. The solid line is a calculated curve. Inset: reciprocal magnetic susceptibilities  $1/\chi$  (closed red circles) and  $1/(\chi - \chi_{VV})$  (blue open circles) in low-temperature region. The thick solid line in the inset is a calculated curve. See text for details.

Figure 2 shows the  $\chi(T)$  curve in the field 1 T along the [001] direction at low temperatures. The magnetic phase transition  $T_N$  is observed at 2.46 K. The temperature dependences of  $\chi(T)$  along the [101] and [111] directions were also measured (not shown here) and they were almost the same as that along the [001] direction at temperatures down to 2 K, implying that  $\chi(T)$  does not show any field-direction dependence even at temperatures below  $T_N$ . However, the absence of the field-direction dependence of  $\chi(T)$  is limited at temperatures in the vicinity of  $T_N$ . The inset in Fig. 2 shows the field dependences of magnetization at 2 K in the fields along the [001], [101], and [111] directions. The magnetization along the [111] direction shows an almost linear dependence against the field, but the magnetizations along the [001] and [101] directions gradually deviate upward slightly from the linear dependence at around 2 T. This result does not indicate that the easy direction of magnetization in fields is parallel to the [001] or [101] direction.

Figure 3 shows the temperature dependences of the specific heat  $C$  of  $\text{SmRh}_2\text{Zn}_{20}$  and  $\text{YRh}_2\text{Zn}_{20}$ . The sharp peak at  $T_N$  is observed at 2.46 K, which is the same temperature as that determined in the  $\chi(T)$  curve. The magnetic component  $C_{\text{mag}}$  of the specific heat is evaluated

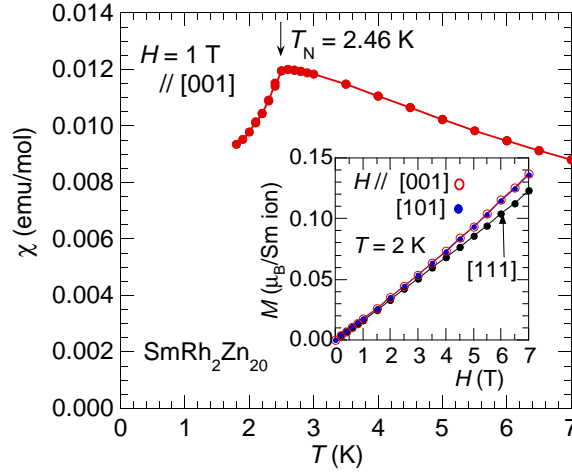


**Fig. 2.** (Color online) Magnetic susceptibility of  $\text{SmRh}_2\text{Zn}_{20}$  in the field 1 T along the [001] direction at temperatures below 7 K. Inset: magnetization curves at 2 K in the fields along the [001], [101], and [111] directions.

as  $C_{\text{SmRh}_2\text{Zn}_{20}} - C_{\text{YRh}_2\text{Zn}_{20}}$  and is shown by the black open circles in this figure. The entropy  $S$  is numerically calculated by integrating  $C/T$  on  $T$  and is shown in the inset in Fig. 3. The entropy at  $T_N$  is approximately equal to  $R \ln 2$ , indicating that the ground state of  $\text{Sm}^{3+}$  is doublet  $\Gamma_7$ . Moreover, the rapid increase in entropy above  $T_N$  with increasing temperature suggests that the excited state  $\Gamma_8$  is close to the ground state. The thick solid line indicated by  $C_{\text{Schottky}}$  in Fig. 3 shows the calculated  $C(T)$  curve of  $\text{SmRh}_2\text{Zn}_{20}$ , where the energy scheme was assumed to be composed of the doublet ground state and the quartet excited state with a gap  $\Delta = 10.8$  K. The solid line indicated by  $S_{\text{Schottky}}$  in the inset is the calculated entropy  $S(T)$  curve. The calculated two lines are in good agreement with the experimental ones above  $T_N$ . This narrow energy gap indicates that the CEF effect is weak, which is consistent with the consideration of the temperature dependence of  $\chi(T)$  above  $T_N$ .  $\chi(T)$  was mostly understood on the basis of the Curie–Weiss law of  $\text{Sm}^{3+}$  without the CEF effect.

Figures 4(a)–4(c) show the temperature dependences of the specific heat of  $\text{SmRh}_2\text{Zn}_{20}$  in magnetic fields along the [001], [101], and [111] directions. Interestingly, in the fields along the [001] and [101] directions,  $T_N$  splits into two and the width of splitting increases with increasing field. The upper  $T_N$  does not change with increasing field, whereas the lower one decreases with increasing field. In the field along the [111] direction,  $T_N$  gradually decreases without splitting. Figure 4(d) shows the field-direction dependence of  $T_N$ . The splitting widths of  $T_N$  at 7 T are 0.26 K in  $H // [001]$  and 0.14 K in  $H // [101]$ . These of  $T_N$  changes appear in the narrow temperature range between 2.16 and 2.46 K.

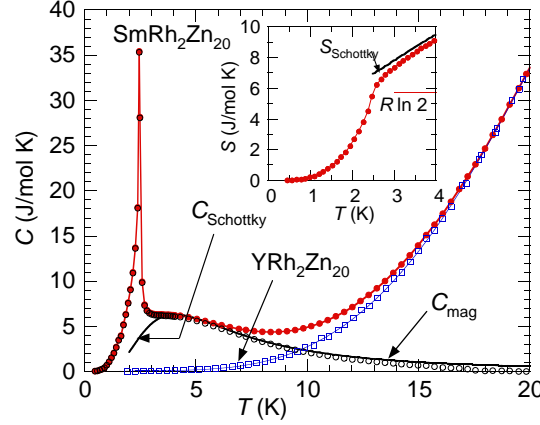


**Fig. 3.** (Color online) Temperature dependences of the specific heat  $C$  of  $\text{SmRh}_2\text{Zn}_{20}$  (red closed circles) and  $\text{YRh}_2\text{Zn}_{20}$  (blue open squares).  $C_{\text{mag}}$  denotes the magnetic part of  $C$  (black open circles) evaluated as  $C_{\text{SmRh}_2\text{Zn}_{20}} - C_{\text{YRh}_2\text{Zn}_{20}}$ . The thick solid line denoted by  $C_{\text{Schottky}}$  is a calculated curve of the Schottky-type specific heat. Inset: temperature dependence of the entropy of  $\text{SmRh}_2\text{Zn}_{20}$ . The solid line denoted by  $S_{\text{Schottky}}$  is a calculated curve. See text for details.

## 4. Analysis and Discussion

### 4.1 Hamiltonian

We discuss the small magnetic anisotropy observed in the magnetization curves at 2 K (inset in Fig. 2), the field-direction dependence of the specific heat  $C(T)$ , and the complex behaviors of  $T_N$  in fields (Fig. 4). Generally, as a consequence of the characteristics of  $\Gamma_7$  and  $\Gamma_8$  of  $\text{Sm}^{3+}$  in the cubic symmetry, the  $\Gamma_7$  state is magnetically isotropic, whereas the  $\Gamma_8$  state is anisotropic in fields. Thus, it is expected that this magnetic anisotropy will be caused by the mixing of the  $\Gamma_8$  state with the ground state  $\Gamma_7$  through the external magnetic field and the exchange field. We analyze this magnetic anisotropy in the frame of the molecular-field approximation. For simplicity, a simple antiferromagnetic structure with two sublattices (A and B) is assumed, that is, the up- and down-magnetic moments are fixed in the A and B sublattices, respectively. We define the following Hamiltonian to analyze the magnetic and thermal properties of  $\text{Sm}^{3+}$  in  $\text{SmRh}_2\text{Zn}_{20}$ ,

$$\mathcal{H}_i = A_4(O_4^0 + 5 O_4^4) + g_J \mu_B \mathbf{J}_i \mathbf{H}_{\text{ext}} + g_J \mu_B \mathbf{J}_i \mathbf{H}_{\text{mol}}(i), \quad (1)$$

where  $i$  denotes the sublattices (A and B). The first term in this equation is the CEF energy,<sup>25–27)</sup> where the six-order term in the CEF energy is excluded because the quantum number  $J$  is  $5/2$ . The mixing effect with the upper multiplet of  $J = 7/2$  will be taken into account by adding  $\chi_{\text{VV}}$  to  $\chi$  calculated using Eq. (1). The second term in Eq. (1) is the Zeeman energy due to the external magnetic field  $\mathbf{H}_{\text{ext}}$ , and the third term is the exchange energy expressed in

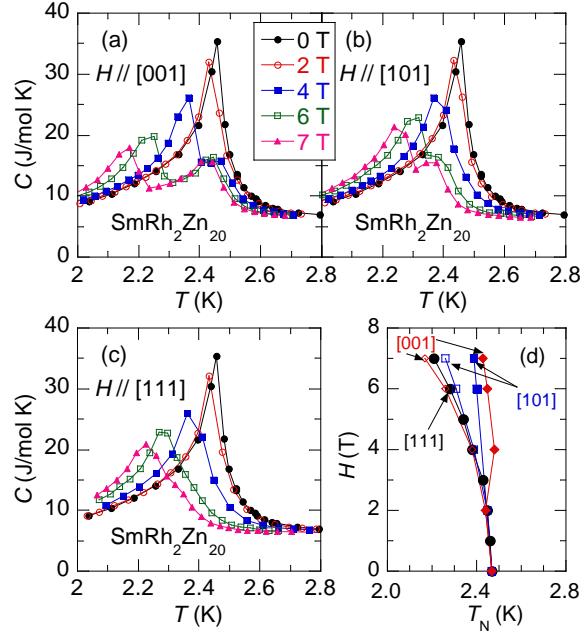


**Fig. 4.** (Color online) Temperature dependences of the specific heat  $C$  of  $\text{SmRh}_2\text{Zn}_{20}$  in magnetic fields along the [001] (a), [101] (b), and [111] (c) directions. (d) Magnetic field dependences of  $T_N$  in the fields along the [001] (filled and open diamonds), [101] (filled and open squares), and [111] (filled circles) directions. See text for details.

the molecular-field approximation. The molecular field  $\mathbf{H}_{\text{mol}}(i)$  at the  $i$  sublattice is expressed using the average magnetic moment in the other sublattice  $j$  as  $n_{\text{BA}}(g_J\mu_B)\langle\mathbf{J}_j\rangle$ , where  $\langle\cdots\rangle$  is the thermal average and  $n_{\text{BA}}$  is the exchange coupling parameter between the atoms in the A and B sublattices. The other parameters used in Eq. (1) are conventionally defined.<sup>25,26)</sup>

The average magnetization at each sublattice is calculated as

$$\mathbf{M}_i = -g_J\mu_B\langle\mathbf{J}_i\rangle = -g_J\mu_B \frac{\text{Tr } \mathbf{J}_i \exp(-\beta\mathcal{H}_i)}{\text{Tr } \exp(-\beta\mathcal{H}_i)}, \quad (2)$$

where  $\beta = 1/k_B T$ . The average magnetization  $\mathbf{M}$  per atom is  $\mathbf{M} = (\mathbf{M}_A + \mathbf{M}_B)/2$ . Note that the physical quantities of  $\mathbf{J}_i$ ,  $\mathbf{H}_{\text{mol}}$ , and  $\mathbf{H}_{\text{ext}}$  are three-dimensional vectors. Thus, Eq. (2) is a set of six equations, which represent the thermal averages of the  $x$ -,  $y$ -, and  $z$ -components of  $\mathbf{M}_A$  and  $\mathbf{M}_B$ . Equation (2) is solved by the iteration method. By using both values of  $\langle\mathbf{J}_A\rangle$  and  $\langle\mathbf{J}_B\rangle$ , which have been obtained using Eq. (2), the specific heat  $C$  per mole is evaluated as

$$C = \left(\frac{N_A}{2}\right) \frac{\partial}{\partial T} \left( \langle\mathcal{H}_A\rangle + \langle\mathcal{H}_B\rangle - \frac{1}{2}\langle\mathcal{H}_{\text{exch}}\rangle \right), \quad (3)$$

where  $N_A$  is Avogadro's number, and the third term in parentheses is used to correct the double counting of the exchange energy between the Sm atoms at A and B sublattices.  $\mathcal{H}_{\text{exch}}$

in this equation is the same as the third term in Eq. (1) and is expressed as  $n_{\text{BA}}(g_J\mu_B)^2\mathbf{J}_A\mathbf{J}_B$ .

We have only two fitting parameters, i.e.,  $A_4$  and  $n_{\text{BA}}$ , when we numerically calculate  $M(T, H)$  and  $C(T, H)$  using the above Hamiltonians, where  $H$  is the magnitude of  $\mathbf{H}_{\text{ext}}$ .  $A_4$  is proportional to  $\Delta$  as  $A_4 = \Delta/360$  in the unit [K], and  $n_{\text{BA}}$  is physically the same as  $n$  [mol/emu] through the relationship of  $n_{\text{BA}} = nN_A$ . As already mentioned in Sect. 3, the energy scheme of  $\text{Sm}^{3+}$  is composed of the doublet ground state  $\Gamma_7$  and the quartet excited state  $\Gamma_8$  with  $\Delta = 10.8$  K. Thus,  $A_4$  is set to be 0.030 [K]. The value of  $n_{\text{BA}}$  was accurately determined to be  $-1.45 k_B/(g_J\mu_B)^2$  by adjusting the calculated  $T_N$  to the experimental  $T_N$ . Consequently, the sublattice magnetic moments  $M_A$  and  $M_B$  are evaluated as a result of the iteration process of Eq. (2) using the two parameters  $A_4$  and  $n_{\text{BA}}$ . This means that the magnetic alignments of each sublattice moment in  $H$  are inferred. First, we present the calculated results of  $\chi(T)$ ,  $M(H)$ ,  $C(T, H)$ , and  $T_N(H)$  in comparison with the respective experimental data in the next subsection. After that, we discuss the magnetic alignments of sublattice magnetic moments in  $H$ .

We have to note one important result concluded from this CEF calculation. At temperatures below  $T_N$ , the magnetic moments at the sublattices are along the  $\langle 111 \rangle$  direction at  $H = 0$ , namely, there exist four magnetic domains below  $T_N$ . For simplicity, we have calculated the  $\chi(T)$ ,  $M(H)$ , and  $C(T)$  curves in fields for a single domain, in which the up- and down-magnetic moments are along the  $[111]$  and  $[\bar{1}\bar{1}\bar{1}]$  directions, respectively.

#### 4.2 Calculation and comparison with the experimental data

Figure 5 shows the calculated temperature dependences of the magnetic susceptibility  $\chi$  of  $\text{SmRh}_2\text{Zn}_{20}$  in the field 1 T along the  $[001]$ ,  $[101]$ , and  $[111]$  directions, where  $\chi$  has been shifted by the amount of  $\chi_{\text{VV}}$  because the mixing effect with the multiplet of  $J = 7/2$  is not taken into account in Eq. (2). In the temperature range between 2 K and  $T_N$ , the magnetic anisotropy is very small, which is consistent with the experimental results. Below 2 K, however, the calculated  $\chi$  shows a magnetic anisotropy, although we cannot compare it with the experimental data, which is limited above 2 K.

The inset in Fig. 5 shows the calculated magnetization curves at 2 K in the fields along the  $[001]$ ,  $[101]$ , and  $[111]$  directions.  $M_{111}(H)$  in  $H \parallel [111]$  increases linearly with increasing field without any anomalies such as spin flops, which is in good agreement with the experimental behavior. On the other hand, the  $M_{101}(H)$  curve deviates slightly from the  $M_{111}(H)$  curve around 3 T, and the  $M_{001}(H)$  curve deviates further from the  $M_{111}(H)$  curve. The characteristic behaviors of the three calculated  $M(H)$  curves at 2 K are in good agreement with



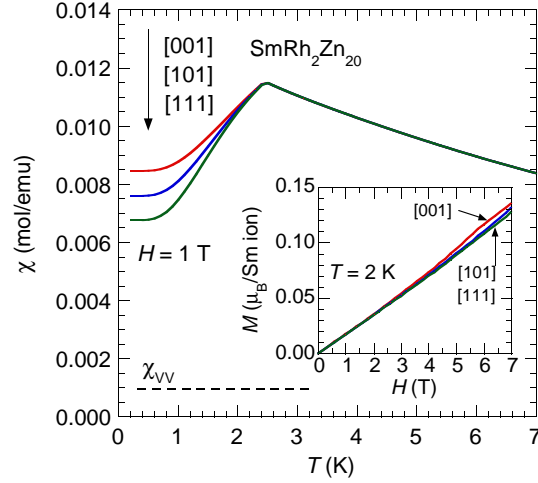


**Fig. 5.** (Color online) Temperature dependences of the calculated magnetic susceptibility of  $\text{SmRh}_2\text{Zn}_{20}$  in the field 1 T along the [001], [101], and [111] directions. Inset: calculated magnetization curves at 2 K along the three directions. See text for details.

the experimental ones.

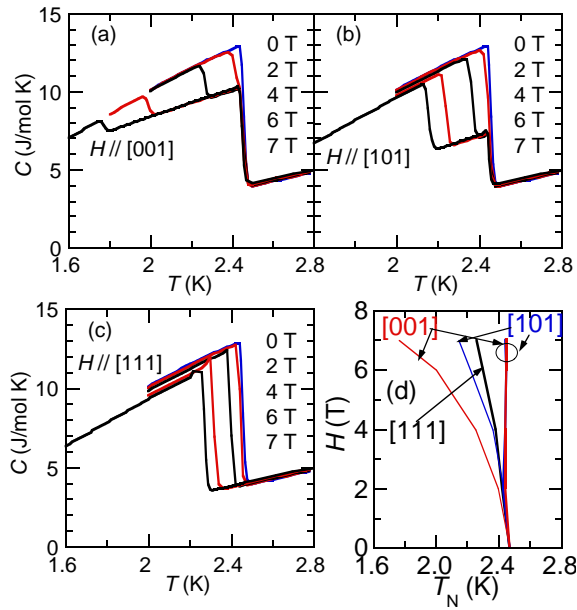


**Fig. 6.** (Color online) Temperature dependences of the calculated specific heat of  $\text{SmRh}_2\text{Zn}_{20}$  in the fields along the [001] (a), [101] (b), and [111] (c) directions. (d) Calculated field dependences of  $T_N$ . See text for details.

Figures 6(a)–6(c) show the calculated specific heat  $C$  in the fields of 0, 2, 4, 6, and 7 T along the [001], [101], and [111] directions. In the case of  $H // [001]$  and [101],  $T_N$  splits into two, and the width of the splitting increases with increasing field. In  $H // [111]$ ,  $T_N$  does not

split but moderately decreases with increasing  $H$ . In Fig. 6(d), the external-field dependences of  $T_N$  are plotted. The splitting widths of  $T_N$  at 7 T are 0.7 K in  $H // [001]$ , 0.3 K in  $H // [101]$ , and zero in  $H // [111]$ . These characteristic behaviors are also in good agreement with the experimental ones. However, note that the height of the calculated specific heat at  $T_N$  at 0 T is one-third compared with that of the experimental specific heat at  $T_N$ , and the second-peak height separated by  $H$  is also lowered compared with the experimental one. This is caused by the fact that the numerical calculation is based on the molecular-field approximation. The magnetic fluctuation  $\langle (\mathbf{J}_A - \langle \mathbf{J}_A \rangle)(\mathbf{J}_B - \langle \mathbf{J}_B \rangle) \rangle$ , which is more important in the vicinity of  $T_N$  than at temperatures far from  $T_N$ , cannot be taken into account in this approximation. In fact, at 2.0 and 2.8 K, which are far below and far above  $T_N$ , respectively, the values of the calculated  $C$  are approximately equal to those of the experimental  $C$ .

It is concluded that the theoretical calculations have successfully reproduced the macroscopic experimental data,  $\chi(T)$ ,  $M(T, H)$ ,  $C(T, H)$ , and  $T_N(H)$ , by using only two parameters,  $A_4$  and  $n_{BA}$ .

#### 4.3 Alignment of sublattice magnetic moments

In this subsection, we present the microscopic magnetic structures of  $\text{SmRh}_2\text{Zn}_{20}$  in the vicinity of  $T_N$ , which have been deduced from the model calculations. Here, we discuss the single magnetic domain.

Figures 7(a)–7(c) show the temperature dependences of the calculated  $x$ -,  $y$ -, and  $z$ -components of the respective sublattice magnetic moments of  $\text{SmRh}_2\text{Zn}_{20}$  in the field 4 T. The subscripts 1 and 2 denote the up- and down-sublattice moments, respectively. In  $H$  along the  $[001]$  direction, as seen in Fig. 7(a), the lower  $T_N$  is found to be the temperature at which the antiferromagnetic alignment along the  $[001]$  direction ( $z$ -component) disappears, and the upper  $T_N$  is the temperature at which the antiferromagnetic alignment of both the  $x$ - and  $y$ -components disappears. In  $H$  along the  $[101]$  direction [Fig. 7(b)], the lower  $T_N$  is the temperature at which the antiferromagnetic alignment along the  $[101]$  direction disappears, and the upper  $T_N$  is the temperature at which the antiferromagnetic alignment of the  $y$ -component disappears. In  $H$  along the  $[111]$  direction [Fig. 7(c)], the magnetizations  $\mathbf{M}_A$  and  $\mathbf{M}_B$  are parallel to the  $[111]$  direction, and the antiferromagnetic alignment disappears at  $T_N$ . Thus, the magnetic susceptibility along the  $[111]$  direction can be considered a parallel magnetic susceptibility. In the cases of  $H$  along the  $[001]$  and  $[101]$  directions, the antiferromagnetic component along the  $H$  directions disappears at temperatures between the lower and upper  $T_N$ 's. Thus, the magnetic susceptibility along these directions can be considered a perpen-

dicular magnetic susceptibility. The lower and upper  $T_N$ 's as well as the  $T_N$  along the [111] direction are second-order phase-transition temperatures.

Figures 8(a)–8(c) show the field dependences of the calculated  $x$ -,  $y$ -, and  $z$ -components of the respective sublattice magnetic moments of  $\text{SmRh}_2\text{Zn}_{20}$  at 2.3 K. In the cases of  $H$  along the [001] and [101] directions, as seen in Figs. 8(a) and 8(b), the antiferromagnetic alignments along the  $H$  directions disappear near 4 and 5 T, respectively. At these points, any anomalous discontinuity such as spin flopping is not theoretically concluded. On the other hand, the antiferromagnetic alignments perpendicular to the  $H$  directions are robust against  $H$  as seen in the figures. In  $H$  along the [111] direction [Fig. 8(c)], the magnetic moments  $\mathbf{M}_A$  and  $\mathbf{M}_B$  are parallel to the  $H$  direction below 6 T. Thus, the magnetization along this direction is due to the parallel susceptibility, as mentioned previously.

The susceptibility  $\chi_{111}$  in  $H$  along the [111] direction has been considered the parallel susceptibility  $\chi_{//}$ . However, as seen in Fig. 5, the calculated  $\chi_{111}(T)$  does not approach zero at 0 K. This behavior is contrary to the common behaviors of usual antiferromagnets. We briefly comment on the discrepancy between the calculated  $\chi_{//}(T)$  and the  $\chi_{//}(T)$  for usual antiferromagnets, although the experimental  $\chi(T)$  is limited above 2 K. In the case of usual antiferromagnets, the sublattice moments  $\mathbf{M}_A$  and  $\mathbf{M}_B$  are saturated at 0 K, and they do not change even if  $H$  is applied; thus,  $\chi_{//}$  is equal to zero. However, when  $\Delta \neq 0$ , the sublattice moments  $\mathbf{M}_A$  and  $\mathbf{M}_B$  are not saturated at 0 K, that is, the moment  $\mathbf{M}_A$  increases and  $\mathbf{M}_B$  decreases with the application of the external field via a Van Vleck-type mechanism between  $\Gamma_7$  and  $\Gamma_8$  states in  $\text{Sm}^{3+}$ ; thus,  $\chi_{//}$  is not equal to zero.

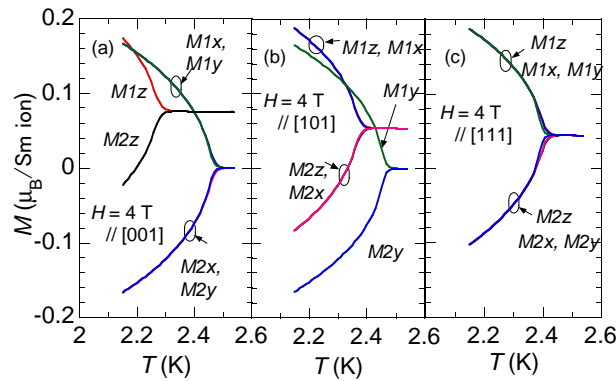


**Fig. 7.** (Color online) Temperature dependences of the calculated  $x$ -,  $y$ -, and  $z$ -components of respective sublattice magnetic moments of  $\text{SmRh}_2\text{Zn}_{20}$  in the field 4 T along the [001] (a), [101] (b), and [111] (c) directions. The subscripts 1 and 2 denote the up- and down-sublattice moments, respectively.

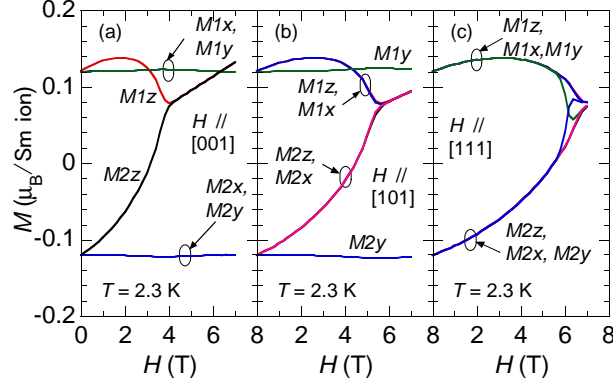


**Fig. 8.** (Color online) Field dependences of the calculated x-, y-, and z-components of respective sublattice magnetic moments of  $\text{SmRh}_2\text{Zn}_{20}$  at 2.3 K in fields along the [001] (a), [101] (b), and [111] (c) directions. The subscripts 1 and 2 denote the up- and down-sublattice moments, respectively.

The microscopic magnetic structures deduced from the theoretical calculations have provided an insight into  $\text{SmRh}_2\text{Zn}_{20}$ . To confirm the magnetic structures of  $\text{SmRh}_2\text{Zn}_{20}$ , neutron scattering experiments should be performed.

#### 4.4 Conclusions

We prepared single crystals of  $\text{SmRh}_2\text{Zn}_{20}$  and measured  $\chi(T)$ ,  $M(T, H)$ , and  $C(T, H)$ . Sm ions in  $\text{SmRh}_2\text{Zn}_{20}$  are in the trivalent state, not in the valence fluctuating state.  $\text{SmRh}_2\text{Zn}_{20}$  is an antiferromagnet with  $T_N = 2.46$  K.  $T_N$  splits into two in  $H // [001]$  and  $[101]$ . The upper  $T_N$  does not change in fields up to the maximum  $H$  of 7 T, whereas the lower  $T_N$  decreases. In  $H // [111]$ ,  $T_N$  does not split and decreases to 2.20 K at 7 T. At 2 K, the magnetization  $M_{111}$  along the [111] direction increases linearly with increasing field, whereas  $M_{001}$  and  $M_{101}$  deviate upward slightly from the linear dependence of  $M_{111}$ . We analyzed these magnetic and thermal properties of  $\text{SmRh}_2\text{Zn}_{20}$  taking into account the CEF effect, Zeeman energy, and exchange interaction. The theoretical calculations have successfully reproduced the experimental  $\chi(T)$ ,  $M(H)$ ,  $C(T, H)$ , and  $T_N(H)$ . The energy scheme of  $\text{Sm}^{3+}$  obtained is composed of the ground state  $\Gamma_7$  and the excited state  $\Gamma_8$  with the energy gap of 10.8 K. The sublattice magnetic moments are along the  $\langle 111 \rangle$  direction below  $T_N$  at  $H = 0$  T. The magnetic structures in magnetic fields in the temperature region between the split  $T_N$ 's could be inferred on the basis of the theoretical calculations.

#### Acknowledgment

We would like to thank K. Nishimura for the critical reading of our manuscript and many useful discussions.

## References

- 1) J. M. Tarascon, Y. Isikawa, B. Chevalier, J. Etourneau, P. Hagenmuller, and M. Kasaya, J. Phys. (Paris) **41**, 1135 (1980).
- 2) J. M. Tarascon, Y. Isikawa, B. Chevalier, J. Etourneau, P. Hagenmuller, and M. Kasaya, J. Phys. (Paris) **41**, 1141 (1980).
- 3) T. Onimaru, K. T. Matsumoto, Y. F. Inoue, K. Umeo, Y. Saiga, Y. Matsushita, R. Tamura, K. Nishimoto, I. Ishii, T. Suzuki, and T. Takabatake, J. Phys. Soc. Jpn. **79**, 033704 (2010).
- 4) N. Nagasawa, T. Onimaru, K. T. Matsumoto, K. Umeo, and T. Takabatake, J. Phys.: Conf. Ser. **391**, 012051 (2012).
- 5) T. Onimaru, N. Nagasawa, K. T. Matsumoto, K. Wakiya, K. Umeo, S. Kittaka, T. Sakakibara, Y. Matsushita, and T. Takabatake, Phys. Rev. B **86**, 184426 (2012).
- 6) M. S. Torikachvili, S. Jia, E. D. Mun, S. T. Hannahs, R. C. Black, W. K. Neils, D. Martien, S. L. Bud'ko, and P. C. Canfield, Proc. Natl. Acad. Sci. U.S.A. **104**, 9960 (2007).
- 7) Y. Isikawa, T. Mizushima, S. Miyamoto, K. Kumagai, M. Nakahara, H. Okuyama, T. Tayama, and T. Kuwai, J. Korean Phys. Soc. **63**, 644 (2013).
- 8) Y. Isikawa, J. Ejiri, T. Mizushima, and T. Kuwai, J. Phys. Soc. Jpn. **82**, 123708 (2013).
- 9) A. Sakai and S. Nakatsuji, Phys. Rev. B **84**, 201106(R) (2011).
- 10) R. Higashinaka, T. Maruyama, A. Nakama, R. Miyazawa, Y. Aoki, and H. Sato, J. Phys. Soc. Jpn. **80**, 093703 (2011).
- 11) A. Yamada, R. Higashinaka, R. Miyazaki, K. Fushiya, T. D. Matsuda, Y. Aoki, W. Fujita, H. Harima, and H. Sato, J. Phys. Soc. Jpn. **82**, 123710 (2013).
- 12) T. Kuwai, T. Furuyama, K. Tada, T. Mizushima, and Y. Isikawa, J. Phys. Soc. Conf. Proc. **3**, 011040 (2014).
- 13) D. Yazici, B. D. White, P.-C. Ho, N. Kanchanavatee, K. Huang, A. J. Friedman, A. S. Wong, V. W. Burnett, N. R. Dilley, and M. B. Maple, Phys. Rev. B **90**, 144406 (2014).
- 14) S. Jia, N. Ni, S. L. Bud'ko, and P. C. Canfield, Phys. Rev. B **80**, 104403 (2009).
- 15) Y. Isikawa, T. Mizushima, J. Ejiri, and T. Kuwai, J. Phys. Soc. Jpn. **83**, 073701 (2014).
- 16) Y. Taga, K. Sugiyama, K. Enoki, Y. Hirose, K. Iwakawa, A. Mori, K. Ishida, T. Takeuchi, M. Hagiwara, K. Kindo, R. Settai, and Y. Onuku, J. Phys. Soc. Jpn. **81**, SB051 (2012).
- 17) M. Tanahashi, K. Adachi, T. Sasahara, N. Kase, T. Nakano, and N. Takeda, Abstr. Meet. Physical Society of Japan (2015 Autumn Meet.), Part 3, p. 1858, 17aPS64 [in Japanese].

- 18) M. Tanahashi, K. Adachi, T. Sasahara, N. Kase, T. Nakano, N. Takeda, Y. Kono, and T. Sakakibara, Abstr. Meet. Physical Society of Japan (2015 Annual Meet.), Part 3, p. 2184, 22aPS94 [in Japanese].
- 19) K. Adachi, T. Sasahara, N. Kase, T. Nakano, and N. Takeda, Abstr. Meet. Physical Society of Japan (2014 Annual Meet.), Part 3, p. 623, 28aPS132 [in Japanese].
- 20) T. Sasahara, T. Nakano, and N. Takeda, Abstr. Meet. Physical Society of Japan (2013 Annual Meet.), Part 3, p. 626, 27aPS69 [in Japanese].
- 21) Y. Isikawa, T. Mizushima, K. Kumagai, and T. Kuwai, J. Phys. Soc. Jpn. **82**, 083711 (2013).
- 22) Y. Isikawa, T. Mizushima, J. Ejiri, S. Kitayama, K. Kumagai, T. Kuwai, P. Bordet, and P. Lejay, J. Phys. Soc. Jpn. **84**, 074707 (2015).
- 23) T. Nasch, W. Jeitschko, and U. C. Rodewald, Z. Naturforsch. B **52**, 1023 (1997).
- 24) S. Jia, N. Ni, G. D. Samolyuk, A. Kracher, K. Dennis, H. Ko, G. J. Miller, S. L. Bud'ko, and P. C. Canfield, Phys. Rev. B **77**, 104408 (2008).
- 25) M. T. Hutchings, Solid State Phys. **16**, 227 (1964).
- 26) K. R. Lea, M. J. M. Leask, and W. P. Wolf, J. Phys. Chem. Solids, **23**, 1381 (1962).
- 27) In the notation of Lea et al.,<sup>26)</sup>  $A_4$  is equal to  $Wx/60$ .